

High-Performance Perovskite Photodetectors Based on CH₃NH₃PbBr₃ Quantum Dot/TiO₂ Heterojunction

Rajeev Ray, Nagaraju Nakka, and Suman Kalyan Pal*

Advanced Materials Research Centre, India Institute of Technology Mandi, Kamand, Mandi-175075, Himachal Pradesh, India.

School of Basic Sciences, India Institute of Technology Mandi, Kamand, Mandi-175075, Himachal Pradesh, India.

AUTHOR INFORMATION

Corresponding Author

*E-mail: suman@iitmandi.ac.in; Phone: +91 1905 267040

ORCID

Suman Kalyan Pal: 0000-0003-2498-6217

Abstract

Organo-lead halide perovskite materials have opened up a great opportunity to develop high performance photodetectors because of their superior optoelectronic properties. The main issue with perovskite-only photodetector is severe carrier recombination. Integration of perovskite with high-conductive materials such as graphene or transition metal sulfides certainly improved the photoresponsivity. However, achieving high overall performance remains a challenge. Here, an improved photodetector is constructed by perovskite quantum dots (QDs) and atomic layer deposited (ALD) ultrathin TiO₂ films. The designed CH₃NH₃PbBr₃ QD/TiO₂ bilayer device displays inclusive performance with on/off ratio of 6.3×10^2 , responsivity of 85 AW⁻¹, and rise/decay time of 0.09/0.11 s. Furthermore, we demonstrate that interface plays a crucial role in determining the device current and enhance the overall performance of heterostructure photodetectors through interface engineering. We believe that this work can provide a strategy to accelerate development of high-performance solution-processed perovskite photodetectors.

Keywords

Perovskite quantum dots, MAPbBr₃, heterojunctions, TiO₂, photodetectors

1. Introduction

Photodetectors are sensors having widespread applications in optical communications, imaging, and chemical/biological sensing ^[1]. At present, photodetectors made of inorganic semiconductors are ruling the markets ^[2]. The main disadvantages of these materials are non-flexibility, high processing cost and not environment-friendly, therefore, an alternative material could be a boon to the electronic industry ^[3]. Organic-inorganic halide perovskites are serious contenders for next-generation photovoltaic technology^[4] owing to their extraordinary optoelectronic properties such as direct bandgap, high absorption coefficients,

low non-radiative Auger recombination, small exciton binding energies and, long lifetime and high mobility of photocarriers^[4c, 5]. Within a very short period (about ten years) the power conversion efficiency (PCE) of perovskite photovoltaic cells has reached 23.7% from 3.81%^[6].

Recently, solution-processed perovskite-based photodetectors have shown great potential in photodetection^[7]. Yang and co-workers reported a vertical perovskite photodetector^[7d] that exhibits excellent light-detecting capability. However, lateral photodetectors are easy to fabricate because of quite a simple device structure; their intrinsic gain mechanism can lead to very high photosensitivity^[8]. The single-layer (lateral) perovskite photodetectors show relatively high detectivity ($\approx 10^{12}$ Jones) and short response time (tens of milliseconds), but, low on/off ratio and poor electrical instability (induced by ion migration)^[7b, 9]. The photocurrent in single-layer perovskite photodetector devices is relatively low because of fast recombination of the photogenerated carriers. These shortcomings are overcome in bilayer devices where perovskite, responsible for light absorption is placed on another material that transports charges. The carrier transport layer underneath the perovskite layer reduces recombination through efficient charge separation at the interface. Significant enhancement of photoresponsivity has been achieved in heterojunctions of perovskite and 2D materials such as graphene, MoS₂^[10], and WS₂^[11]. Graphene-based photodetectors^[9c, 11a-d] offer very low on/off ratio, whereas detectors with MoS₂ possess low rise and decay times^[11e, 11f].

Perovskite quantum dot (QD) based photodetectors are being quickly developed as well. Wang et al.^[7a] fabricated bilayer photodetectors with all-inorganic perovskite QDs and mesoporous TiO₂. Epitaxially blended CH₃NH₃PbBr₃ (MAPbBr₃) QDs and ternary PbS_xSe_{1-x} QDs have been used as active layer in photodetectors^[12]. However, the performance of perovskite QD based photodetectors is limited by low photoresponsivity. In this article, we

have fabricated MAPbBr₃QD/TiO₂ heterojunction on FTO substrate for photodetection. Mesoporous TiO₂ films have been prepared via atomic layer deposition (ALD) technique for better transport of photocarriers. The fabricated bilayer devices exhibit excellent performance in terms of photoresponsivity and response time. The performance of the photodetector is found to be highly dependent on the quality of the perovskite/TiO₂ interface. Moreover, UV-ozone treatment of the TiO₂ layer improves the detector performance.

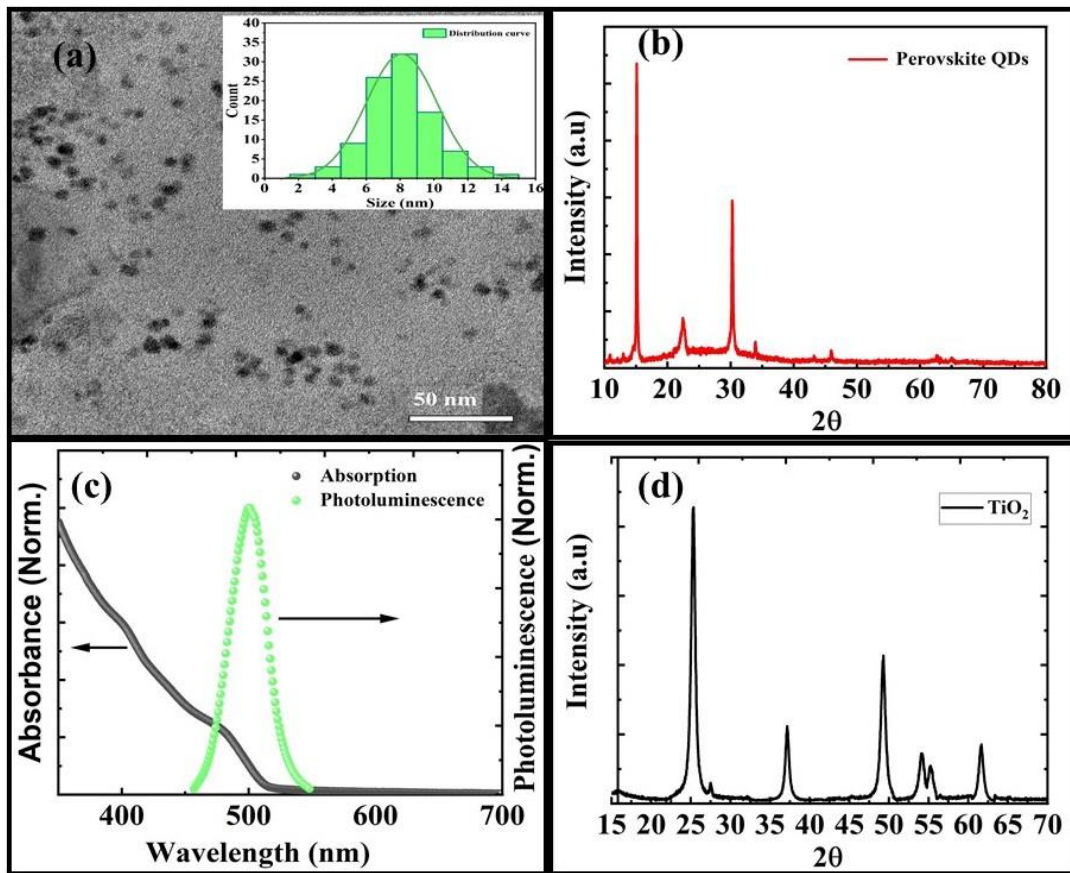


Figure 1. (a) TEM image of MAPbBr₃ QDs. The inset shows the particle size distribution of MAPbBr₃ QDs. (b) XRD spectrum of MAPbBr₃ QD film. (c) Absorption and PL spectra of MAPbBr₃ QD films. (d) XRD pattern of TiO₂ thin film prepared through ALD.

2. Results and Discussion

2.1. Characterization of MAPbBr₃ QDs and TiO₂ Thin Film

We prepared MAPbBr₃ QDs using facile solution process, which is given in the Experimental Section. The TEM image of perovskite QDs is illustrated in Figure 1a. It is seen from the inset of Figure 1a that the size of QDs is ~ 7.5 nm. Figure 1b depicts the X-ray diffraction (XRD) spectrum of the perovskite film. All the peaks (at 14.9°, 23.8°, 31.2°, and 46.04°) observed in the XRD spectrum are well matched to the tetragonal perovskite structure. No impurity peaks are observed other than those attributed to MAPbBr₃. The light absorption spectrum of MAPbBr₃ QD film is shown in Figure 1c. QDs exhibit strong absorption in the UV and visible light range with a peak at 490 nm. A strong PL is emitted from QDs at 520 nm (Figure 1c). The narrow FWHM of the PL band suggests uniform size distribution of QDs, which is also apparent from the TEM histogram (Figure 1a). The absorption edge of mesoporous TiO₂ was appeared at 388 nm (not shown) indicating bandgap energy of 3.2 eV. Figure 1d shows XRD pattern of ALD-TiO₂ film (annealed). The presence of 2θ peaks at 25.27° and 48.01° validates the anatase phase formation in TiO₂ films.

2.2. Single Layer vs Bilayer Devices

When MAPbBr₃ QD/TiO₂ heterojunction is used as the active material in photodetectors, the photoelectrical performance is significantly enhanced. Figure 2a presents the schematic device structure for MAPbBr₃ QD/mesoporous TiO₂ heterojunction photodetector on patterned FTO coated substrate. To demonstrate the superiority of heterojunction photodetectors, two devices: only TiO₂ (PDR) and MAPbBr₃ QD/TiO₂ (PD1) were fabricated. The thickness of the TiO₂ layer was 50 nm in both the devices. Figure 2b shows the symmetric waterfall type I-V characteristics of the photodetectors suggesting ohmic contact between TiO₂ film and electrodes, which is essential for good photoconductor and

photodetector devices [13]. The dark current of the device PDR measured at 5 V is quite low; in the order of nanoampere. It is even lower in the heterojunction device PD1 because of the formation of a low-conductive depletion region at the perovskite /TiO₂ heterojunction. The photocurrent of PD1 increases dramatically up to 0.3 μA (at 5 V), which is more than one order of magnitude higher than that of PDR (Figure 2b). The low photocurrent in PDR can be

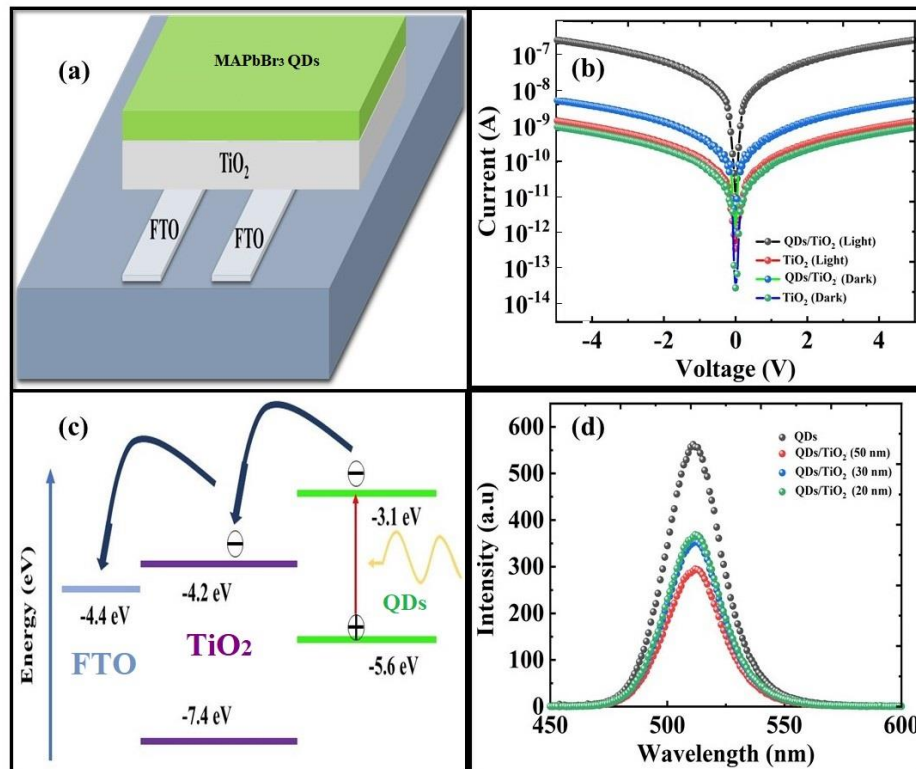


Figure 2. (a) Schematic representation of the structure of MAPbBr₃ QD/TiO₂ heterojunction photodetectors. (b) I-V curves of only TiO₂ (PDR) and MAPbBr₃ QD/TiO₂ heterojunction (PD1) photodetectors (in dark and under light illumination). Current is plotted in log scale. (c) Band diagram of different layers of the heterojunction device demonstrating the electron transfer process under light illumination. (d) PL quenching of perovskite QDs in the presence of TiO₂ layer (thicknesses 50, 30 and 20 nm).

explained from the fact that TiO₂ absorbs less light in the visible region due to very high bandgap as mentioned before. On the other hand, in the bilayer device, a large number of

photocarriers is generated in the perovskite layer upon light illumination because of its strong absorption in the visible light range. As shown in figure 2c, MAPbBr₃/TiO₂ heterojunction possesses type II band alignment that causes photogenerated electrons to transfer into the underlying TiO₂ film by spatially separating them from photogenerated holes. The separation of photogenerated carriers via electron transfer can reduce carrier recombination leading to low PL from perovskite QDs. It is proved strongly from the PL quenching of perovskite QDs (Figure 2d) that the recombination of electron-hole pairs in QD film is suppressed due to the electron transfer to TiO₂ layer. The injection of electron into TiO₂ can enhance the conductivity of the TiO₂ layer, which is the key requirement behind high-performance of heterojunction photodetectors.

2.3. MAPbBr₃ QD/TiO₂ Heterojunction Photodetectors

In addition to PD1, two more devices having thickness of TiO₂ layer 30 nm (PD2) and 20 nm (PD3) were fabricated. Similar XRD pattern (Figure 1d) of TiO₂ films of varying thickness (50, 30 and 20 nm) infers that there was no crystallographic change of the TiO₂ layer with the change of thickness. The photoresponses of all three devices are presented in Figure 3a-c. The device PD1 produces the highest photocurrent (6.5×10^{-7} A), while the lowest photocurrent (4.4×10^{-7} A) is obtained from PD3. The photocurrents of all the fabricated photodetectors are consistent and reproducible. The on/off ratio of the three devices PD1, PD2 and PD3 are found to be 5.54×10^2 , 5.0×10^2 and 3.7×10^2 , respectively.

The transient photocurrent behaviour of a photodetector can be understood through the response (rise or decay) time, which is one of the essential performance parameters. The rise time (T_r) is defined as the transition time of the photocurrent from 10% to 90% of the peak value, while the decay time (T_d) is the time taken to decrease the photocurrent from 90% to 10% of the peak value^[14]. Transient photoresponse curves for all three devices are provided

in Figure S1 (Supporting Information). The response time of the fabricated devices is calculated and presented in Table 1. Clearly, the response of our perovskite QD photodetector is much faster than recently reported values [15].

Another important photoelectric characteristic of a photodetector is the responsivity (R), which can be defined as electrical output per optical input [16].

$$R = \frac{\Delta I}{PS} \quad (1)$$

where $\Delta I = I_{\text{on}} - I_{\text{off}}$, P is the power density of the incident light, and S is the effective area under light exposure. The responsivity is found to be 65, 54 and 45 AW^{-1} for PD1, PD2 and PD3 devices, respectively (Table 1).

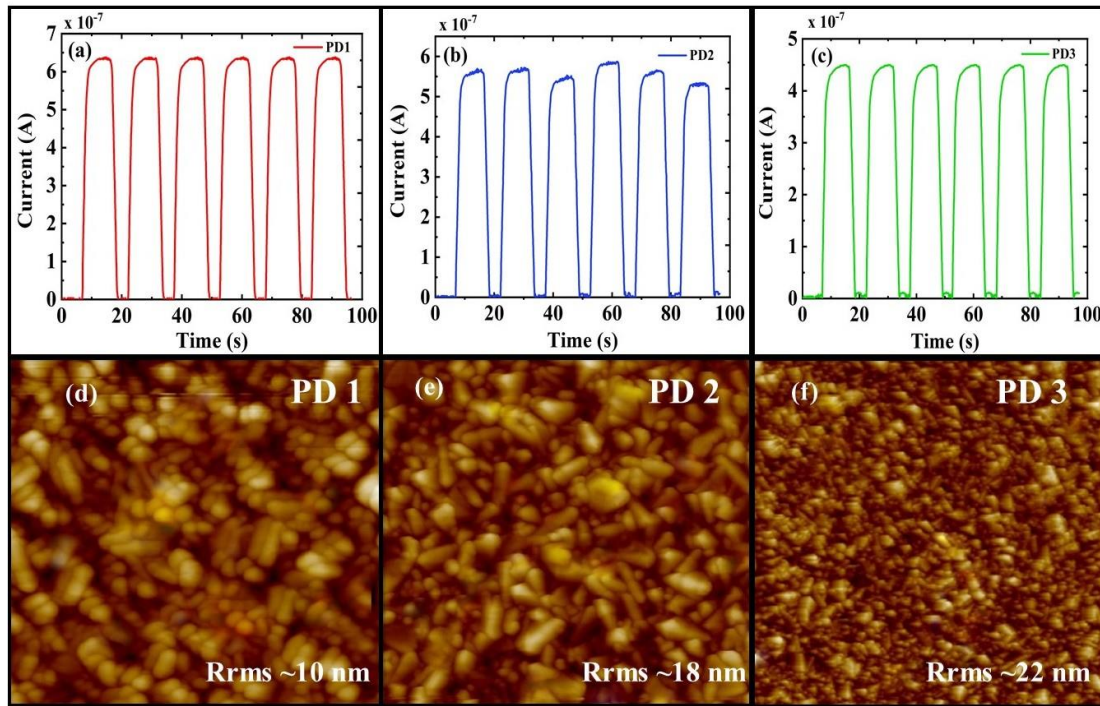


Figure 3: (a-c) ON and OFF photoresponsive cycles of three different heterojunction photodetectors. (d-f) AFM images showing surface roughness of TiO_2 films of different thicknesses (50, 30 and 20 nm).

It is evident from Table 1 that the overall performance of the bilayer photodetectors depends on thickness of the TiO₂ layer and the device PD1 exhibits highest performance. Usually surface roughness of ALD grown TiO₂ film is thickness dependent ^[17]. The AFM images of TiO₂ films having thicknesses 50, 30 and 20 nm are shown in Figure 3d-f. The values of surface roughness of these films are 10, 18 and 22 nm, respectively. Clearly, surface roughness varies with the thickness of TiO₂ film. Nonetheless, the quenching of PL intensity of MAPbBr₃ QDs is more for TiO₂ layer of 50 nm thickness (Figure 2d) suggesting much efficient transfer of electrons to the TiO₂ film of lowest roughness. The roughness induced surface traps at the interface hinder the electron injection from perovskite to TiO₂^[17]. Hence, the efficiency of the electron injection to TiO₂ layer increases with reduction of roughness of the interface. The improved electron injection increases the electrical conductivity of the TiO₂ layer and finally leads to highest photocurrent in the device with thickest TiO₂ layer.

Table 1: Performance parameters of heterojunction photodetectors (PD1, PD2 and PD3)

Device	Rise time (s)	Decay time (s)	Responsivity (A W ⁻¹)	On/Off ratio
PD1	0.14	0.14	65	550
PD2	0.20	0.15	54	500
PD3	0.23	0.15	45	370

2.4. Effect of Surface Treatment on the Performance of Heterojunction Photodetectors

The accumulation of hydrocarbons on the rough surface of the TiO₂ layer could deteriorate the quality of the interface affecting the charge transfer across the interface ^[18]. Several surface treatments such as compact or blocking layer^[19], scattering layer^[20], atomic doping^[21]

of the TiO₂ films have been testified to enhance solar cell efficiency by improving the interface quality. Treatment with TiCl₄ has been applied quite often to increase the efficiency of solar cells and optoelectronic devices^[22]. However, TiCl₄ is not stable at room temperature as it reacts with moisture present in the air to produce the harmful hydrochloric acid^[23]. It is also observed that oxygen ion beam treatment is efficient than oxygen plasma treatment for improving solar cell performance^[24]. The main drawback of oxygen plasma treatment is the requirement of considerable capital investment. However, UV-ozone (O₃) treatment is an effective and economical surface treatment method^[25]. To examine the effect UV-O₃ treatment, we fabricated a photodetector with UV-O₃ treated TiO₂ layer (thickness 50 nm). The I-V characteristics of the device was measured and is presented in Figure S2 (Supporting Information). Time-dependent photocurrent and transient photoresponse curves (measured at 5 V) for ozone untreated and treated photodetectors are presented in figure 4a-c. The treated device exhibits on/off ratio, responsivity and rise/decay time of 630, 85 WA⁻¹ and 0.09/0.11 s, respectively (Table 2). Undoubtedly, the perovskite QD/TiO₂ device displays very high overall performance following the UV-ozone treatment of the TiO₂ layer. Recent advancements on the perovskite-based heterojunction photodetectors is summarized in Table S1 (Supporting Information). In comparison to the recent progress, our MAPbBr₃ QD/TiO₂ heterojunction photodetector has significant advantages over response time and photoresponsivity.

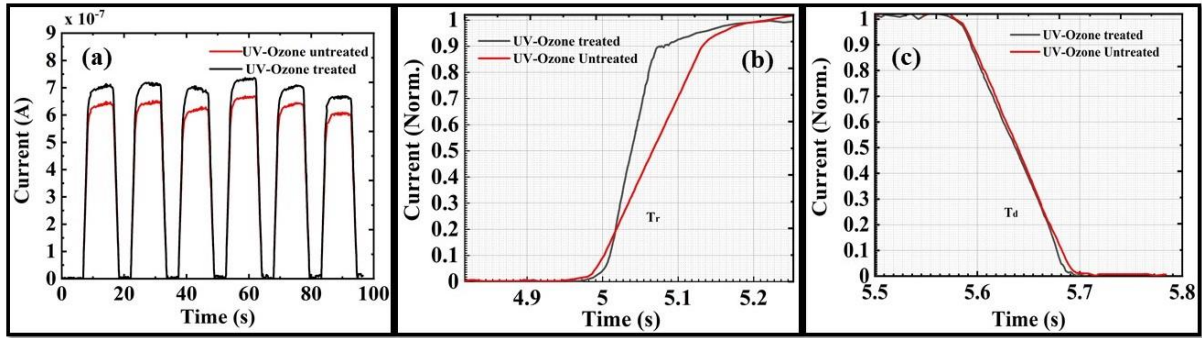


Figure 4. (a) Current vs. time graph of UV-ozone treated and untreated photodetectors at 5V. (b-c) Transient photocurrent response (rise/decay time) of ozone-treated and untreated photodetectors.

Table 2: Performance parameters of photodetectors before and after ozone treatment

Device	Rise time (s)	Decay time (s)	Responsivity (AW^{-1})	On/Off ratio
Ozone untreated	0.14	0.14	65	550
Ozone treated	0.09	0.11	85	630

To understand the effect of UV-ozone treatment, X-ray photoemission spectroscopy (XPS) measurements have been performed for untreated and treated TiO_2 films. Figure 5a and b show the C1s peaks of TiO_2 films. The intensity of C1s peak at 284.8 eV is found to be reduced after UV- O_3 treatment. The quantitative analysis of peaks reveals that the area under C-C peak is decreased after UV- O_3 treatment. Clearly, UV- O_3 treatment burns out organic contaminants present on the surface of TiO_2 film^[26] and thereby clean the surface of the film. The O1s peak at 530.1 eV (Figure 5c-d) is associated with oxygen bonding to coordinatively saturated titanium atoms (lattice oxygen of TiO_2). The signal at higher binding energy (531.5 eV) could be attributed to the formation of Ti^{3+} surface states through the creation of oxygen vacancies, which is normally inscribed as Ti_2O_3 ^[23]. The ratio between the numbers of oxygen

atoms present was estimated by comparing areas under Ti_2O_3 peaks and found to be increase from 8.2% to 15.4% after the UV- O_3 treatment. Therefore, the change of oxidation state from Ti^{4+} to Ti^{3+} takes place through the introduction of negative oxygen species (O^-) on the surface of TiO_2 during UV- O_3 exposure [18b, 26b, 27]. Oxygen vacancies generated during the reduction of Ti^{4+} to Ti^{3+} produces electrons, which affect the surface functionality and charge state of the TiO_2 film. The additional electrons generated by UV- O_3 treatment improve the carrier transport property of TiO_2 film resulting high photocurrent and fast response of the photodetectors. Nonetheless, because of less carbon contaminants, more perovskite QDs could be adsorbed on the TiO_2 surface by refining the quality of the heterojunction.

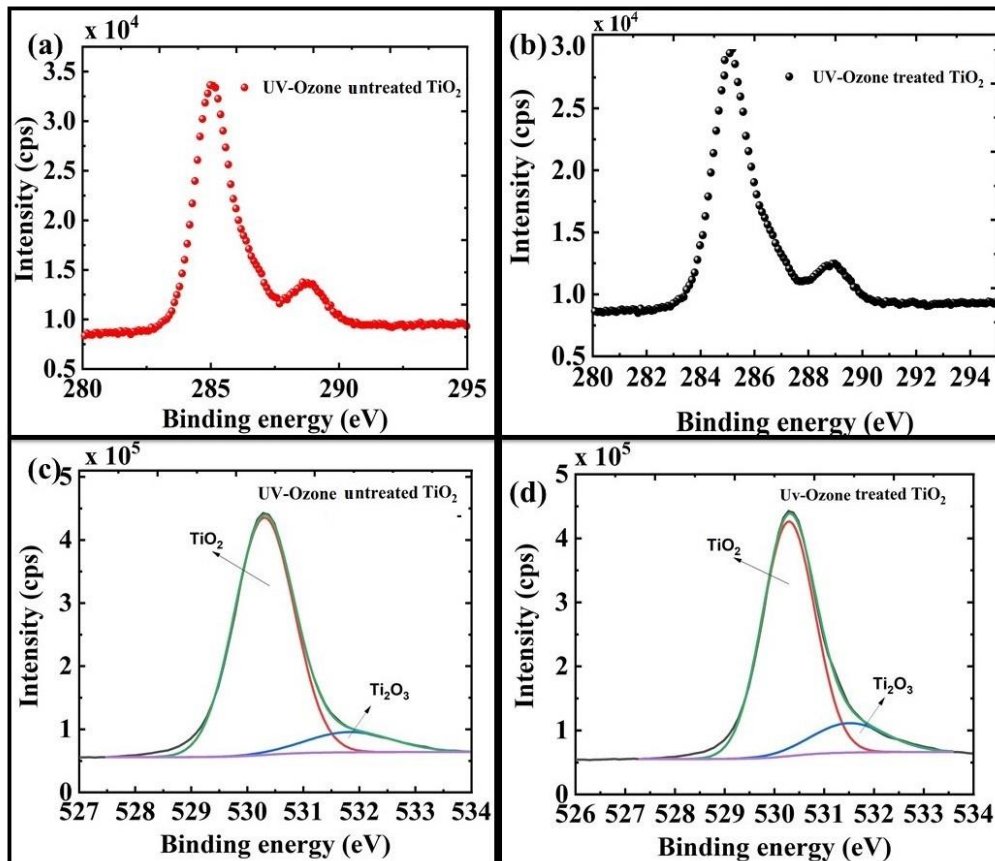


Figure 5. XPS spectra of TiO_2 films on FTO glass substrates. (a, c) untreated and (b, d) UV-ozone treated TiO_2 films. Gaussian/Lorentzian peak fitting technique is used to identify the contribution of individual species.

3. Conclusion

In summary, MAPbBr₃ QD/TiO₂ heterojunction photodetectors were fabricated using atomic layer deposited ultra-thin TiO₂ films. Due to the improved conductivity of TiO₂ layer through the efficient extraction of electrons at the interface, the performance of heterojunction photodetectors is increased. The performance of such photodetectors depends on the interface quality and the device having lowest interface roughness offers highest performance. UV-ozone treatment of the TiO₂ layer enhances the device performance by improving both the interface quality and conductivity of the TiO₂ layer. The heterojunction device exhibits high responsivity of 85 AW⁻¹, and short rise/decay time of 0.09/0.11 s. In comparison to the reported perovskite-based heterojunction photodetectors, the MAPbBr₃ QD/TiO₂ device exhibits very high overall performance. Our findings could be beneficial to developing perovskite-based flexible heterojunction photodetectors.

4. Experimental Methods

Materials: All chemicals were used without further purification. Lead (II) bromide (PbBr₂, 99%, Sigma Aldrich), methylamine (CH₃NH₂, Sigma Aldrich), hydrochloric acid (HCl, 37 wt % in water, Sigma Aldrich), hydrobromic acid (HBr, 48 wt % in water, Sigma Aldrich), oleic acid (Sigma Aldrich), N,N-dimethylformamide (Sigma Aldrich) were used for the preparation of perovskite QDs.

Synthesis of MAPbBr₃ QDs: Methylammonium bromide (CH₃NH₃Br) was prepared through a reaction of methylamine in ethanol with HBr at room temperature. HBr was added dropwise while stirring. Upon drying at 100 °C, a white powder of CH₃NH₃Br was formed. The powder was dried overnight in a vacuum oven and purified with ethanol. To obtain highly

green luminescent perovskite QDs, $\text{CH}_3\text{NH}_3\text{Br}$ and PbBr_2 were dissolved in anhydrous dimethylformamide (DMF).

Device fabrication: Photodetectors were fabricated on laser patterned fluorine-doped tin oxide (FTO) coated glass substrates (sheet resistivity $7 \Omega/\text{cm}^2$) with a channel length of $5 \mu\text{m}$. First, substrates were cleaned by ultrasonication in a soap solution, deionized water, acetone, and isopropanol, respectively. The cleaned FTO substrates were baked for 30 minutes before ozone treatment. Then, the ultra-thin layer of TiO_2 was deposited by atomic layer deposition (ALD) on FTO at 150°C . The thickness of the TiO_2 films was controlled by varying the deposition cycles. Then perovskite QD films were deposited on the TiO_2 layer by spin coating at a speed of 700 rpm for 30 s. The fabricated devices were annealed at 100°C to enhance the device performance by improving the quality of $\text{MAPbBr}_3\text{QD}/\text{TiO}_2$ interface.

Measurements: Synthesized QDs were characterized by absorption and photoluminescence (PL) spectroscopy using Shimadzu UV-2450 spectrometer and Cary Eclipse spectrophotometer from Agilent Technologies, respectively. The dimension of the QDs was estimated from transmission electron microscopy (TEM) using TECNAI G2 200 kV (FEI, Electron Optics) electron microscope. X-ray diffraction (XRD) was performed in a Smart Lab, RIGAKU 9 kW rotating anode diffractometer. The surface morphology and thickness of compact TiO_2 layer were characterized using atomic force microscopy (Dimension Icon from Bruker) in tapping mode at room temperature and ellipsometry (Accurion EP4), respectively. Current-voltage (I-V) characteristics and photodetection measurements were carried out using a class 3A solar simulator (OAI TriSOL) fitted with an AM (air mass) 1.5 filter for light exposure and equipped with a Keithley 2400 source meter unit. We performed X-ray photoelectron spectroscopy (XPS) in a SPECS instrument with a PHOIBOS 100/150 detector (DLD) at 385 W, 13.85 kV, 39.6 nA (sample current), and a pass energy of 50 eV. Curve synthesis and deconvolution, i.e., identifying the components of the XPS signals, were

performed by fitting the XPS signal with Gaussian/Lorentzian function. The binding energies were calibrated using the C1s peak for adventitious carbon at a binding energy of 284.5 eV, with an associated error of $\pm 0.1-0.2$ eV.

Supporting Information

Supporting Information is available from the Wiley Online Library or from the author.

Acknowledgements

The experimental facilities in Advanced Materials Research Centre are greatly acknowledged. R.R. and N.N are thankful to IIT Mandi for their fellowship.

References

- [1] a) F. P. G. de Arquer, A. Armin, P. Meredith, E. H. Sargent, *Nat. Rev. Mater.* **2017**, 2, 1; b) L. H. Zeng, Q. M. Chen, Z. X. Zhang, D. Wu, H. Yuan, Y. Y. Li, W. Qarony, S. P. Lau, L. B. Luo, Y. H. Tsang, *Adv. Sci.* **2019**, 6, 1901134.
- [2] a) Q. Yang, Q. Wu, W. Luo, W. Yao, S. Yan, J. Shen, *Mater. Res. Express.* **2019**, 6, 116208; b) N. Kumar, K. Arora, M. Kumar, *J. Phys. D* **2019**, 52, 335103; c) I. Kumari, S. Das, A. Bag, *Selective UV Detection by AlGaIn/GaN-Based MSM Photo Detector for Integration with Silicon*, **2018**, *IEEE SENSORS, New Delhi*, pp. 1.
- [3] a) M. I. H. Ansari, A. Qurashi, M. K. Nazeeruddin, *J. Photochem. Photobiol. C* **2018**, 35, 1; b) J. Sun, J. Wu, X. Tong, F. Lin, Y. Wang, Z. M. Wang, *Adv. Sci.* **2018**, 5, 1700780.
- [4] a) P. S. Chandrasekhar, A. Dubey, Q. Qiao, *Sol. Energy* **2020**, 197, 78; b) R. Ray, A. S. Sarkar, S. K. Pal, *Sol. Energy* **2019**, 193, 95; c) N.-G. Park, M. Grätzel, T. Miyasaka, K. Zhu, K. Emery, *Nat. Energy.* **2016**, 1, 1.

- [5] a) D. Bi, W. Tress, M. I. Dar, P. Gao, J. Luo, C. Renevier, K. Schenk, A. Abate, F. Giordano, J.-P. C. Baena, *Sci. Adv.* **2016**, 2, e1501170; b) S. Ghosh, S. K. Pal, K. J. Karki, T. Pullerits, *ACS Energy Lett.* **2017**, 2, 2133.
- [6] H.-S. Kim, A. Hagfeldt, N.-G. Park, *ChemComm* **2019**, 55, 1192.
- [7] a) L. Zhou, K. Yu, F. Yang, J. Zheng, Y. Zuo, C. Li, B. Cheng, Q. Wang, *Dalton Trans.* **2017**, 46, 1766; b) Y. Zhang, J. Du, X. Wu, G. Zhang, Y. Chu, D. Liu, Y. Zhao, Z. Liang, J. Huang, *ACS Appl. Mater. Inter.* **2015**, 7, 21634; c) L. Dou, Y. Yang, J. You, Z. Hong, W.-H. Chang, G. Li, Y. Yang, *Nat. Commun.* **2014**, 5, 5404; d) L. Dou, Y. M. Yang, J. You, Z. Hong, W.-H. Chang, G. Li, Y. Yang, *Nat. Commun.* **2014**, 5, 5404.
- [8] C. Musca, J. Siliquini, B. Nener, L. Faraone, *IEEE Trans. on Electron Devices* **1997**, 44, 239.
- [9] a) X. Hu, X. Zhang, L. Liang, J. Bao, S. Li, W. Yang, Y. Xie, *Adv. Funct. Mater.* **2014**, 24, 7373; b) H. Lu, W. Tian, F. Cao, Y. Ma, B. Gu, L. Li, *Adv. Funct. Mater.* **2016**, 26, 1296; c) K. C. Kwon, K. Hong, Q. Van Le, S. Y. Lee, J. Choi, K. B. Kim, S. Y. Kim, H. W. Jang, *Adv. Funct. Mater.* **2016**, 26, 4213.
- [10] R. Ray, A. S. Sarkar, S. K. Pal, *J. Phys. D* **2020**, 53, 275109.
- [11] a) Y. Lee, J. Kwon, E. Hwang, C. H. Ra, W. J. Yoo, J. H. Ahn, J. H. Park, J. H. Cho, *Adv. Mater.* **2015**, 27, 41; b) Y. Wang, Y. Zhang, Y. Lu, W. Xu, H. Mu, C. Chen, H. Qiao, J. Song, S. Li, B. Sun, *Adv. Opt. Mater.* **2015**, 3, 1389; c) M. Spina, M. Lehmann, B. Náfrádi, L. Bernard, E. Bonvin, R. Gaál, A. Magrez, L. Forró, E. Horváth, *Small* **2015**, 11, 4824; d) Z. Sun, L. Aigouy, Z. Chen, *Nanoscale* **2016**, 8, 7377; e) C. Ma, Y. Shi, W. Hu, M. H. Chiu, Z. Liu, A. Bera, F. Li, H. Wang, L. J. Li, T. Wu, *Adv. Mater.* **2016**, 28, 3683; f) D. H. Kang, S. R. Pae, J. Shim, G. Yoo, J. Jeon, J. W. Leem, J. S. Yu, S. Lee, B. Shin, J. H. Park, *Adv. Mater.* **2016**, 28, 7799; g)

- Y. Wang, R. Fullon, M. Acerce, C. E. Petoukhoff, J. Yang, C. Chen, S. Du, S. K. Lai, S. P. Lau, D. Voiry, *Adv. Mater.* **2017**, 29, 1603995.
- [12] M. Sulaman, S. Yang, Y. Jiang, Y. Tang, B. Zou, *Nanotechnology* **2017**, 28, 505501.
- [13] Y. Dang, G. Tong, W. Song, Z. Liu, L. Qiu, L. K. Ono, Y. Qi, *J. Mater. Chem. C* **2020**, 8, 276.
- [14] W. Tian, T. Zhai, C. Zhang, S. L. Li, X. Wang, F. Liu, D. Liu, X. Cai, K. Tsukagoshi, D. Golberg, *Adv. Mater.* **2013**, 25, 4625.
- [15] a) J. Lu, A. Carvalho, H. Liu, S. X. Lim, A. H. Castro Neto, C. H. Sow, *Angew. Chem.* **2016**, 128, 12124; b) R. K. Upadhyay, A. P. Singh, D. Upadhyay, A. Kumar, C. Kumar, S. Jit, *IEEE Electron Device Lett.* **2019**, 40, 1961; c) R. K. Upadhyay, A. P. Singh, D. Upadhyay, S. Ratan, C. Kumar, S. Jit, *IEEE Photon. Technol.* **2019**, 31, 1151; d) L. Zhou, K. Yu, F. Yang, H. Cong, N. Wang, J. Zheng, Y. Zuo, C. Li, B. Cheng, Q. Wang, *J. Mater. Chem. C* **2017**, 5, 6224; e) X. Yi, Z. Ren, N. Chen, C. Li, X. Zhong, S. Yang, J. Wang, *Adv. Electron. Mater.* **2017**, 3, 1700251.
- [16] a) H. Wang, D. H. Kim, *Chem Soc Rev* **2017**, 46, 5204; b) Z. Zheng, F. Zhuge, Y. Wang, J. Zhang, L. Gan, X. Zhou, H. Li, T. Zhai, *Adv. Funct. Mater.* **2017**, 27, 1703115.
- [17] A. E. Shalan, S. Narra, T. Oshikiri, K. Ueno, X. Shi, H.-P. Wu, Mahmoud M. Elshanawany, E. Wei-Guang Diao, H. Misawa, *Sustain. Energy & Fuels* **2017**, 1, 1533.
- [18] a) B.-K. Lee, J.-J. Kim, *Curr. Appl. Phys.* **2009**, 9, 404; b) Z. Wang, J. Fang, Y. Mi, X. Zhu, H. Ren, X. Liu, Y. Yan, *Appl. Surf. Sci.* **2018**, 436, 596.
- [19] A. Sangiorgi, R. Bondoni, N. Sangiorgi, A. Sanson, B. Ballarin, *Ceram. Int.* **2014**, 40, 10727.

- [20] Z. A. Garmaroudi, M. Abdi-Jalebi, M. R. Mohammadi, R. H. Friend, *RSC Adv.* **2016**, 6, 70895.
- [21] S. Thogiti, J. Y. Park, C. T. Thanh Thuy, D. K. Lee, B.-K. Min, H. J. Yun, J. H. Kim, *ACS Sustain. Chem. Eng.* **2018**, 6, 13025.
- [22] a) H. Park, W.-R. Kim, H.-T. Jeong, J.-J. Lee, H.-G. Kim, W.-Y. Choi, *Sol Energ. Mat. Sol C* **2011**, 95, 184; b) B. C. O'Regan, J. R. Durrant, P. M. Sommeling, N. J. Bakker, *J. Phys. Chem. C* **2007**, 111, 14001.
- [23] K. Qi, S.-y. Liu, Y. Chen, B. Xia, G.-D. Li, *Sol Energ. Mat. Sol C* **2018**, 183, 193.
- [24] M. K. Parvez, G. M. Yoo, J. H. Kim, M. J. Ko, S. R. Kim, *Chem. Phys. Lett.* **2010**, 495, 69.
- [25] F. Egitto, L. Matienzo, *J. Mater. Sci.* **2006**, 41, 6362.
- [26] a) K.-H. Park, M. Dhayal, *Electrochem. commun.* **2009**, 11, 75; b) H. Liu, W. Yang, Y. Ma, Y. Cao, J. Yao, J. Zhang, T. Hu, *Langmuir* **2003**, 19, 3001.
- [27] a) Y. Chu, H. Cai, L. Huang, Z. Xing, Y. Du, J. Ni, J. Li, J. Zhang, *Phys. Status. Solidi. A.* **2019**, 216, 1800669; b) X. Zhang, H. Tian, X. Wang, G. Xue, Z. Tian, J. Zhang, S. Yuan, T. Yu, Z. Zou, *Mater. Lett.* **2013**, 100, 51.

Supporting Information

High-Performance Perovskite Photodetectors Based on $\text{CH}_3\text{NH}_3\text{PbBr}_3$ Quantum Dot/ TiO_2 Heterojunction

Rajeev Ray, Nagaraju Nakka, and Suman Kalyan Pal*

Advanced Materials Research Centre, India Institute of Technology Mandi, Kamand, Mandi-175075, Himachal Pradesh, India.

School of Basic Sciences, India Institute of Technology Mandi, Kamand, Mandi-1750075, Himachal Pradesh, India

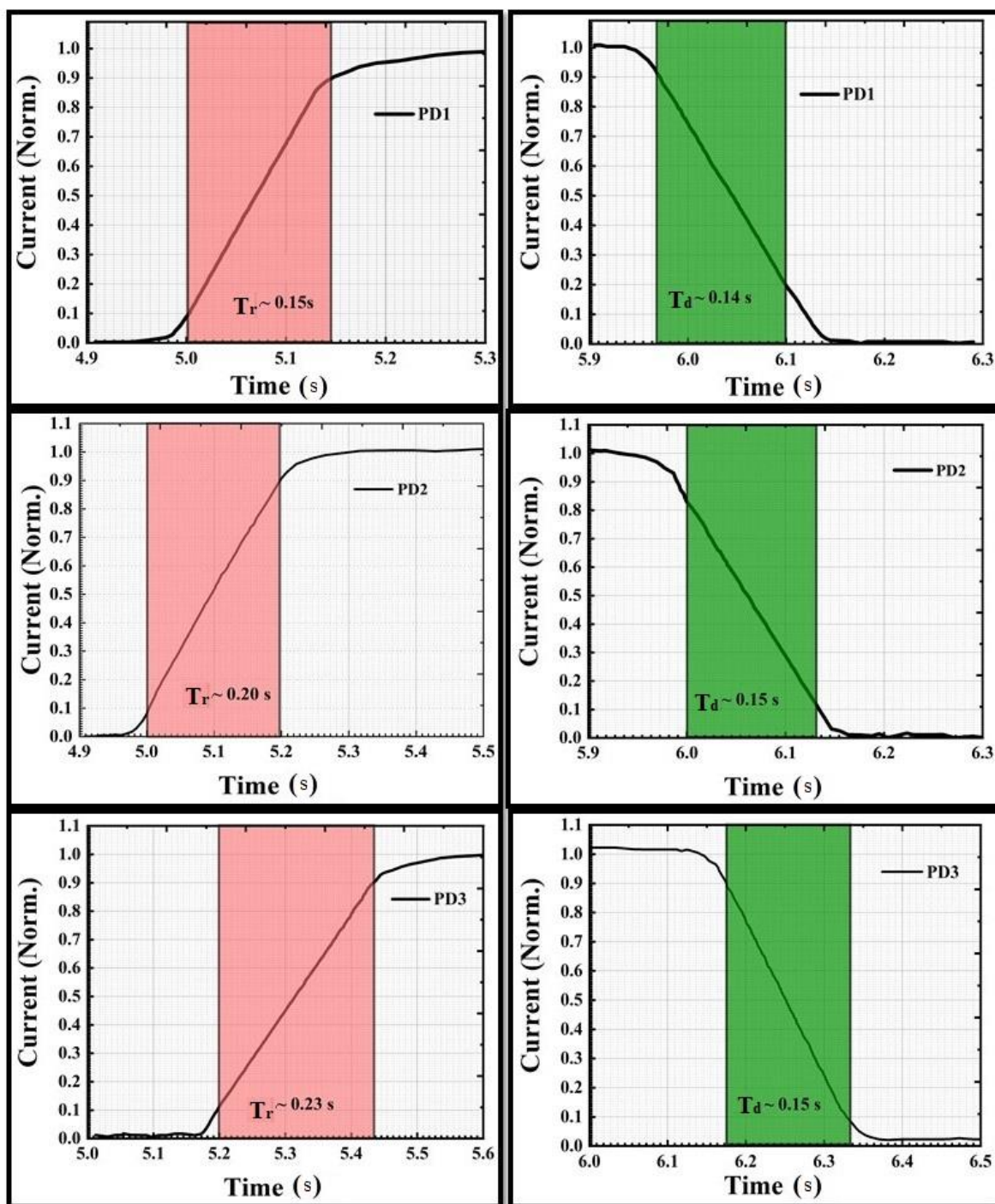


Figure S1. Transient photocurrent response of MAPbBr₃ QD/TiO₂ heterojunction photodetectors (PD1, PD2 and PD3) under white light illumination at a bias of 5 V.

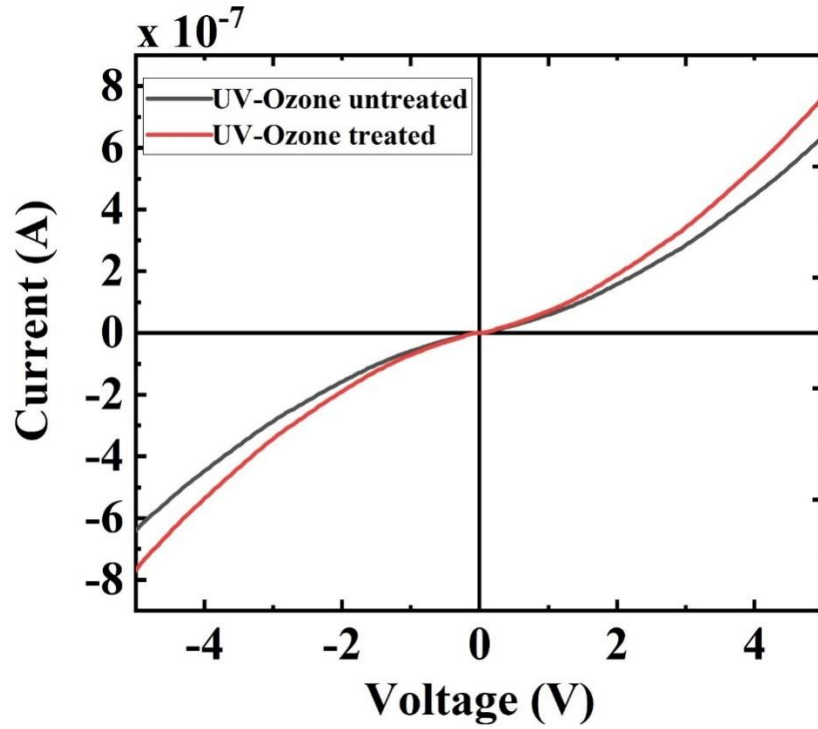


Figure S2. I-V characteristics of a photodetector fabricated with UV-ozone untreated and treated TiO₂ layer.

Table S1. Comparison of response time and responsivity of perovskite-based photodetectors

Device structure	Rise time (s)	Decay time (s)	Responsivity (A W ⁻¹)	Ref.
TiO ₂ /MAPbBr ₃	0.02	0.02	0.49×10^{-6}	[1]
WSe ₂ /MAPbI ₃	2	2	110	[2]
BiFeO ₃ /CH ₃ NH ₃ PbI ₃	0.74	0.09	2.0	[3]
ZnO/MAPbI ₃	NA	NA	21.8	[4]
CsPbBr ₃ -MPA (mp-TiO ₂)	4.7	2.3	24.5	[5]
TiO ₂ Nanocrystal/MAPbBr ₃	0.49	0.56	0.12	[6]
ZnO NCs/PbS _x Se _{1-x} QDs / MAPbBr ₃ QDs	NA	NA	16.65	[7]
ALD TiO ₂ /MAPbBr ₃ QDs	0.09	0.11	85.0	This work

References

- [1] H.-R. Xia, J. Li, W.-T. Sun, L.-M. Peng, *ChemComm* **2014**, 50, 13695.
- [2] J. Lu, A. Carvalho, H. Liu, S. X. Lim, A. H. Castro Neto, C. H. Sow, *Angew. Chem.* **2016**, 128, 12124.
- [3] R. K. Upadhyay, A. P. Singh, D. Upadhyay, A. Kumar, C. Kumar, S. Jit, *IEEE Electron Device Lett.* **2019**, 40, 1961.
- [4] R. K. Upadhyay, A. P. Singh, D. Upadhyay, S. Ratan, C. Kumar, S. Jit, *IEEE Photon. Technol.* **2019**, 31, 1151.
- [5] L. Zhou, K. Yu, F. Yang, H. Cong, N. Wang, J. Zheng, Y. Zuo, C. Li, B. Cheng, Q. Wang, *J. Mater. Chem. C* **2017**, 5, 6224.
- [6] X. Yi, Z. Ren, N. Chen, C. Li, X. Zhong, S. Yang, J. Wang, *Adv. Electron. Mater.* **2017**, 3, 1700251.
- [7] M. Sulaman, S. Yang, Y. Jiang, Y. Tang, B. Zou, *Nanotechnology* **2017**, 28, 505501.